Journal of Materials Chemistry A



PAPER

View Article Online
View Journal | View Issue



Cite this: J. Mater. Chem. A, 2021, 9, 15238

Embryonic zeolite-assisted synthesis of SSZ-13 with superior efficiency and their excellent catalytic performance†

Linying Wang,^a Dali Zhu,^{ab} Juan Wang,^{ac} Wenhao Cui,^{ab} Jingfeng Han,^a Bing Li,^a Dong Fan, ^{ba} Peng Tian*^a and Zhongmin Liu ^{b*abc}

An X-ray amorphous material with a CHA-like structure, named embryonic CHA zeolite, has been designed and employed for the synthesis of SSZ-13, which leads to ultra-fast crystallization (1.5–12 h), wide product SiO_2/Al_2O_3 ratio (SAR = 22–100) and high yield (82.8–92.9%). The usage of N,N,N-trimethyl-1-adamantammonium hydroxide (TMAdaOH) for the synthesis can be controlled at unprecedentedly low amounts (TMAdaOH/SiO $_2$ = 0.035–0.050). Characterization results reveal that the embryonic zeolite has a small particle size of 10–20 nm, large micro/mesopore volume and abundant double 6-ring units (subunits of the CHA structure). It provides ample active surface and subunits for the formation of the CHA structure and promotes the fast synthesis of SSZ-13 with a wide phase region. The resultant material (SAR = 23.2), after Cu $^{2+}$ exchange, exhibits superior NH $_3$ -SCR activity and extraordinary hydrothermal stability (steaming at 800 °C for 16 h), implying its promising application for NO $_x$ removal. In addition, high-silica SSZ-13 shows good catalytic performance for the MTO reaction. It is anticipated that the embryonic zeolite-assisted strategy will benefit the synthesis of more industrially important zeolites.

Received 18th February 2021 Accepted 12th June 2021

DOI: 10.1039/d1ta01452h

rsc.li/materials-a

Introduction

Zeolites with inorganic crystalline frameworks have been widely used in industry because of their well-defined micropores and cavities, adjustable surface acidity and good thermal stability.¹⁻³ The development of zeolite synthesis strategies facilitates the creation of novel zeolitic materials, the improvement of synthetic efficiency and the fine tuning of zeolite physicochemical properties, which would prompt the practical application of zeolites.⁴⁻⁶

SSZ-13, a high-silica counterpart of natural chabasie, belongs to the ABC-6 family of zeolites with three-dimensional channels (0.38 \times 0.38 nm) and large ellipsoidal cages (0.67 \times 1 nm). It has caught considerable attention because of its promising catalytic performance in the conversion of methane to methanol,⁷⁻⁹ selective catalytic reduction of NO $_x$ by NH $_3$ (NH $_3$ -SCR)¹⁰⁻¹³ and methanol-to-olefin (MTO) reactions.^{14,15} Previous studies have demonstrated that SSZ-13 with a relatively low

 SiO_2/Al_2O_3 ratio (SAR ~ 20) is desirable for the NH₃-SCR reac-

Hitherto, the most powerful organic structure-directing agent (OSDA) for the formation of high-silica SSZ-13 has been TMAdaOH, which, however, is highly expensive and leads to high product cost. A great deal of effort has been made for the synthesis of SSZ-13 over the past decades. 16-22 After extensive exploration, the usage of TMAdaOH for the crystallization of SSZ-13 with a lower SAR is currently reduced to OSDA/SiO₂ \approx 0.1.16 However, for high silica SSZ-13, a large amount of TMAdaOH (OSDA/SiO₂ \geq 0.2) is still necessary, even involving the use of toxic fluoride ions. 15,23,24 This is likely due to the increased growth barrier of the high-silica framework. Besides the direct synthesis, an inter-conversion methodology (using zeolites such as FAU, GIS or beta as the precursor) was also developed. 25-27 But the use of the zeolite precursor increases the complexity of the synthetic procedure and hinders its scale-up. In addition, several alternative OSDAs have also been discovered for the synthesis of SSZ-13. Unfortunately, most of them only exert the structure directing effect under inter-conversion conditions, 28-34 and all of them lead to SSZ-13 products with narrow and low SARs. Hitherto, the efficient and cost-effective synthesis of SSZ-13 with a controllable SAR has still remained a challenging task.

tion after Cu²⁺ exchange, as it can provide a large amount of acid sites to adsorb NH₃ molecules.¹¹ However, for the MTO reaction, high silica SSZ-13 becomes an appropriate choice, because lower acid density can abate the hydrogen-transfer reaction and coke deposition (deactivation).¹⁵

[&]quot;National Engineering Laboratory for Methanol to Olefins, Dalian Institute of Chemical Physics, Chinese Academy of Sciences, Dalian, 116023, China. E-mail: tianpeng@dicp.ac.cn; liuzm@dicp.ac.cn

^bUniversity of Chinese Academy of Sciences, Beijing 100049, China

^cZhang Dayu School of Chemistry, Dalian University of Technology, Dalian, 116024, China

[†] Electronic supplementary information (ESI) available. See DOI: 10.1039/d1ta01452h

X-ray amorphous zeolitic materials (regarded as zeolite precursors or embryonic zeolites) have attracted increasing attention in recent years.35-37 They possess zeolitic acidity/ oxidation, large external surface area and enhanced accessibility of active sites, leading to improved catalytic activity. Such advantages become more evident when they are utilized for reactions involving large molecules. Spectroscopic characterizations have demonstrated that the Si and Al (Ti) atoms in the amorphous materials have a short-range order and the microstructures of the materials are in close similarity to the crystallized products. But the lack of long-range order makes these materials X-ray amorphous.

Given the high external surface area and abundant building units of the X-ray amorphous zeolite precursors, it is envisioned that besides catalytic applications, such materials may have a powerful effect on promoting the crystallization of zeolites as effective nuclei, as they could provide a vast amount of building units with open accessibility and promote the nucleation and crystallization. Herein, for the first time we designed and prepared an X-ray amorphous material with a CHA-like structure (named embryonic CHA zeolite) and explored its effect on the synthesis of SSZ-13. It was found that the embryonic zeolite has superior activity in inducing the crystallization of SSZ-13, which allows the successful synthesis under an extremely low usage of TMAdaOH together with a rapid crystallization rate and wide product SAR. NH₃-SCR and MTO reactions were chosen to test the catalytic performance of the obtained SSZ-13.

Experimental

Materials

The chemical reagents used for the experiments included: sodium aluminate (48 wt% Al₂O₃, 36 wt% Na₂O, Aladdin), mesoporous silica gel (99 wt%, Qingdao Meigao Reagent Co.), tetraethyl-orthosilicate (TEOS, 99 wt%, Kermel), aluminium isopropoxide (≥98 wt%, Aladdin), sodium hydroxide (NaOH, 99.9 wt%, Aladdin), N,N,N-trimethyl-1-adamantammonium hydroxide (TMAdaOH, 25 wt% in H2O, Annaiji), ammonium nitrate (NH₄NO₃, 99 wt%, Beijing Chemical Reagent Co., Ltd), and copper acetate monohydrate (Cu(CH₃COO)₂·H₂O, 99 wt%, Tianjin Damao Chemical Reagent Co.).

Preparation of embryonic-CHA-zeolite solution

0.39 g aluminum isopropoxide was added into TMAdaOH solution (6.08 g TMAdaOH solution in 7.10 g H₂O) under stirring to form a clear solution. Then, TEOS (5.00 g) was dropwise added to obtain a final gel. After stirring for 4 h, the gel was placed into a stainless autoclave and heated under rotation (45 rpm) at 140 °C for 14 h. The prepared solution is referred to as embryonic-CHA-zeolite solution, which is used for the following preparation of SSZ-13 zeolite without solid-liquid separation.

Embryonic zeolite-assisted synthesis of SSZ-13 zeolite

Sodium aluminate, NaOH, TMAdaOH and deionized water were mixed to form a clear solution before the addition of the silica gel. After stirring for 5 minutes, a given amount of embryonic-

CHA-zeolite solution was added into the gel (10 wt% addition based on silica) under stirring to form a gel with the composition of 1 SiO₂: 1/x Al₂O₃: 0.048 Na₂O: y TMAdaOH: 20.6 H₂O, where x ranges from 20 to 100 and y ranges from 0.035 to 0.050. The gel was then charged into a 30 mL autoclave with a Teflon liner. The reaction was carried out under rotation (45 rpm) at 175-205 °C for a few hours. Then the solid was separated by filtration, washed, and dried at 110 °C overnight. The sample was named SSZ-13_m, where m presents the product SiO_2/Al_2O_3 ratio detected by XRF.

Characterization

A PANalytical X'Pert PRO X-ray diffractometer (Cu Kα radiation) was employed to collect the powder X-ray diffraction (PXRD) data. The inorganic elemental compositions were determined with an X-ray fluorescence (XRF, Philips Magix-601) spectrometer. The crystal morphology was observed using a scanning electron microscope (SEM, Hitachi SU8020). HRTEM images were obtained on a transmission electron microscope (TEM, JEM-2100). The textural properties were measured by N2 sorption at -196 °C on a Micromeritics ASAP2020 volumetric adsorption analyzer. Before the measurement, the sample was pretreated at 350 °C for 360 minutes. Thermal gravimetric analyses (TG-DTG) were performed on a NETZSCH ATS 449 F3 analyzer from 33 to 900 $^{\circ}$ C with a heating rate of 10 $^{\circ}$ C min⁻¹. The UV-Vis spectrum was collected on a UV-Vis-NIR spectrophotometer (Varian Cary 5000) and BaSO₄ was employed as the background. UV-Raman spectra were collected using a homemade single stage UV-Raman spectrograph with the resolution of 2 cm⁻¹, the single-frequency UV laser line was 244 nm and the output of the exciting source was 10 mW. The power of the laser at the sample was about 2 mW. The solid-state NMR experiments were carried out on a BrukerAvance III 600 spectrometer, which is equipped with a 14.1 T wide-bore magnet using a 4 mm WVT double resonance MAS probe. The chemical shifts of ²⁹Si, ²⁷Al and ¹³C were referenced to Kaolinite at -91.5 ppm, NH₄Al(SO₄)₂·12H₂O at -0.4 ppm and adamantine at 38.5 ppm. The liquid 13C NMR analysis was performed on a Bruker Avance III 400 using D2O as the deuterated reagent.

Catalyst preparation

The NH₄-form sample was obtained by ion exchange of the calcined sample with NH₄NO₃ solution (1.0 M, liquid/solid = 15) at 80 °C, each time is 2 h for a total of three times. The Cuform sample was prepared by ion exchange of the NH₄-form sample two times with Cu(CH₃COO)₂ solution (0.20 wt%, liquid/solid = 50) at 80 °C, and each time is 2 h, followed by filtration and washing. All the ion-exchanged samples are dried at 100 °C for 12 h. The final solid was calcined in an air atmosphere at 550 °C for 300 minutes to remove the organics. The Cu content of Cu-SSZ-1323.2 was determined by XRF.

Catalytic test

The NH₃-SCR reaction was performed in a fixed-bed quartz reactor.38 For a detailed test, 0.30 g Cu-SSZ-13 and 1.90 g quartz beads (60-80 mesh) were mixed uniformly and loaded into the reactor. The catalyst was firstly heated in N_2 to 550 °C, and then the temperature was kept constant for 0.5 h in the presence of the feed gas before the reaction. A Fourier transform infrared spectrometer (Bruker) was chosen to detect the concentration of NO, NO₂, and N₂O. The following formula was used to determine the NO_x conversion:

$$= \frac{(\text{ [NO]}_{\text{in}} - \text{[NO]}_{\text{out}} - \text{[NO_2]}_{\text{out}} - 2\text{[N_2O]}_{\text{out}})}{\text{[NO]}_{\text{in}}} \times 100\%$$

MTO reaction was tested in a fixed-bed reactor. 0.30 g H-SSZ-13 (40–60 mesh) was transferred into the reactor before the catalyst was activated at 550 °C for 1 h (N_2 as the carrier gas). The feed methanol was imported by passing N_2 (40.0 mL min⁻¹) through a saturator containing methanol at 35 °C. The final products were analysed with a gas chromatograph (Agilent, GC7890, FID detector and Poraplot Q-HT capillary column).

High-temperature (HT) hydrothermal treatment

The catalyst was hydrothermally treated at 750 or 800 $^{\circ}$ C for 16 h in the presence of 12.5% H_2O in air with a GHSV of 90 000 h⁻¹.

Results and discussion

Physicochemical properties of embryonic CHA zeolite

Fig. 1a presents the powder XRD pattern of the solid separated from the prepared embryonic-CHA-zeolite solution. No diffraction peaks are observed, indicating the X-ray amorphous feature of the solid. The TEM image shown in Fig. 1b reveals that the solid is composed of uniform nanoparticles in the size of 10–

20 nm. No lattice fringes can be discerned, which implies the absence of crystallites and is in agreement with the XRD result. The N₂ isotherms of the solid are displayed in Fig. 1c, which present a type of I + IV isotherms with an obvious hysteresis loop in the range of $P/P_0 = 0.7-1.0$, suggesting the coexistence of micropores and meso/macropores in the sample. In view of the TEM result, the meso/macropores should originate from the void space of adjacent nanoparticles. The large external surface area (220 m² g⁻¹) and meso-macropore volume (0.77 cm³ g⁻¹) observed for the solid also agree well with its small particle size. Moreover, the micropore size distribution curve gives a much broad peak with maximum at 0.55 nm, which is larger than that of the well-crystallized SSZ-1334.1 (inset in Fig. 1c). The micropore volume and micropore surface area of the solid sample are $0.10 \text{ cm}^3 \text{ g}^{-1}$ and $203 \text{ m}^2 \text{ g}^{-1}$, respectively, indicating its highly microporous structure.39

Fig. 1d shows the ¹³C MAS NMR spectrum of the solid. Four well-resolved resonances attributed to the TMAda⁺ cation are clearly observed, evidencing the intact inclusion of TMAda⁺ in the solid.³³ TG-DTG curves (Fig. 1e) further reveal that the amorphous solid contains 25 wt% TMAda⁺, which is larger than that (16 wt%) in the as-made SSZ-13_{34.1}. Moreover, the OSDA decomposition temperature (200–650 °C) in the solid is much broader than that in SSZ-13_{34.1} (400–650 °C). This implies that the local environments of OSDA cations in the amorphous solid are more complex and part of OSDA cations have relatively weak interactions with the aluminosilicate species.³⁵

UV Raman is usually chosen to probe the zeolite structure because it is quite sensitive to the framework/ring vibrations in zeolites.^{39,40} It is especially powerful in supplying structural information even for amorphous materials in the induction

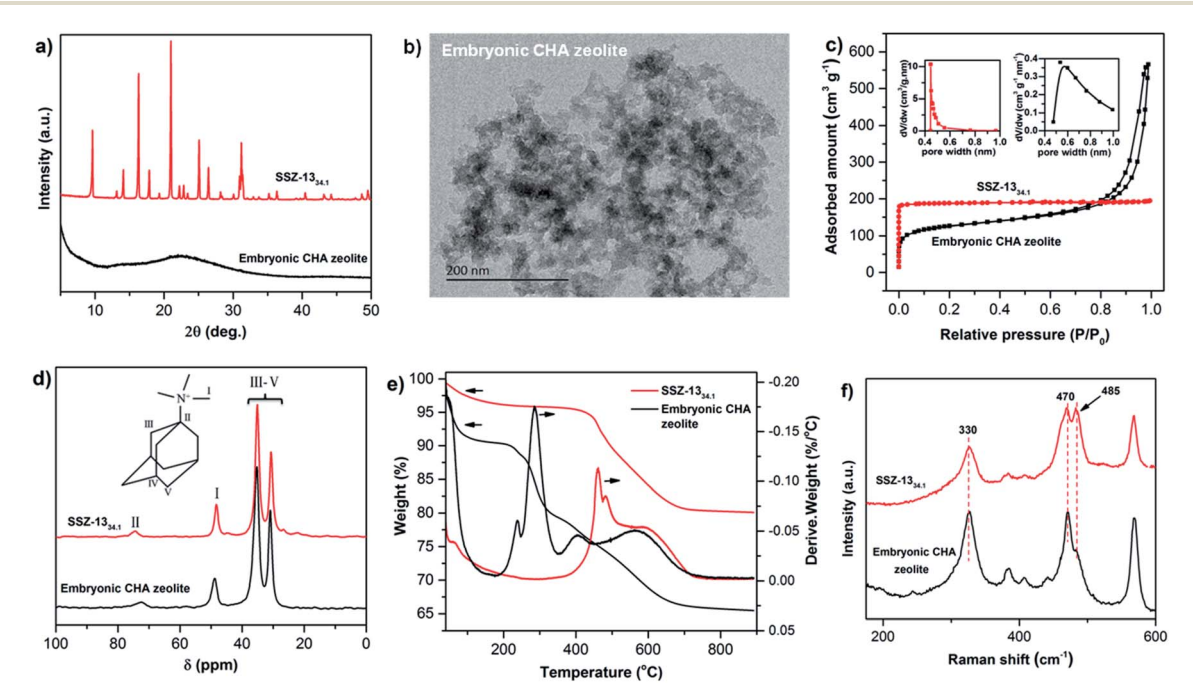


Fig. 1 (a) XRD patterns, (b) TEM image, (c) N_2 sorption isotherms (insets show the distribution of micropores), (d) 13 C MAS NMR, (e) TG-DTG curves and (f) UV-Raman spectra of the samples. As-made samples for (a), (b) and (d-f); calcined sample for (c).

period of zeolite crystallization. Fig. 1f presents the UV-Raman spectrum of the solid. For comparison, the UV-Raman spectrum of SSZ-13 is also shown in the figure. The strong band at 330 cm⁻¹ is assigned to D6R in the CHA structure. The band at 470 cm⁻¹ accompanied by a shoulder at 485 cm⁻¹ can be ascribed to the 4R in the CHA framework. 41,42 Other bands in the spectra are mainly related to the TMAda⁺ cation. Overall, the UV-Raman spectra of the solid and SSZ-13 have high similarity.

Based on the above characterizations, it is clear that the amorphous solid recovered from the prepared solution has the characteristics of nanometer size, abundant micropores and D6R units, although a large-scale three-dimensional crystalline structure has not yet been developed. Considering that D6R is the most important composite building unit for the formation of the CHA structure and the solution can yield the SSZ-13 product after a prolonged heating time (Fig. S1†), the amorphous solid is therefore named embryonic CHA zeolite to show its close relationship with the CHA structure.

Embryonic zeolite-assisted synthesis of SSZ-13

The embryonic-CHA-zeolite solution was directly employed for the synthesis of SSZ-13. There are two advantages in doing so: (1) there is no need for solid separation; (2) the residual OSDA in the solution can be further utilized for the synthesis. The representative synthesis results are summarized in Table 1. Clearly, SSZ-13 can be obtained in a wide range of gel SARs and the corresponding product SAR increases from 23.2 to 96.1. The OSDA usage for the synthesis of the sample SSZ-13_{23.2} is as low as $OSDA/SiO_2 = 0.035$, which is an unprecedentedly low TMAdaOH dosage for the SSZ-13 synthesis. Following the increase of gel SAR, more OSDA (OSDA/SiO $_2 = 0.04-0.05$) is needed to reach complete crystallization, suggesting the incremental difficulty in the formation of the high-silica CHA framework. To learn the utilization efficiency of TMAda⁺ in the synthesis, the mother liquid of SSZ-1334.1 recovered after crystallization was analyzed by ¹³C NMR. As shown in Fig. S2,† no signals assigned to TMAda⁺ can be discerned, implying its complete consumption.

Moreover, all the embryonic zeolite-assisted syntheses are complete in a short time (12 h) at 175 °C with a high solid yield of 82.8-92.9%. The crystallization time could be even shortened dramatically to 1.5 h (sample SSZ-1331.5) when the temperature increased from 175 to 205 °C. Such a wide range of crystallization temperature might be owing to its ultra-low gel alkalinity $(OH^-/SiO_2 = 0.137)$, which allows the OSDA to play its role in a dominant manner and avoids the formation of the impurity phase. In addition, the ultra-low gel alkalinity should also contribute to the high solid yield of the synthetic system by decreasing the dissolution of silica.43 On the other hand, as a recent study revealed that the indispensable premise of the fast crystal growth is to form high ordering nuclei,44 it is speculated that embryonic zeolites might first promote the fast formation of ordering CHA nuclei, which leads to the ultrafast crystallization rate of SSZ-13 in this work. Apparently, the strategy developed herein is highly efficient for the synthesis of SSZ-13, characteristic of ultra-low OSDA dosage, wide phase region, high yield and fast crystallization rate.

To verify the powerful effect of the embryonic-CHA-zeolite solution for the crystallization of SSZ-13, two groups of contrast experiments with different gel SARs were conducted, including without the addition of embryonic-zeolite solution (contrast A) and the use of H-SSZ-13 seeds in place of the embryonic-zeolite solution (contrast B). The chosen seed has a similar composition to that of the embryonic-CHA-zeolite solution and the detailed parameters are shown in Fig. S3[†] (XRD and SEM). Detailed synthesis parameters for the contrast experiments are summarized in Table S1.† The corresponding XRD patterns and SEM images of the contrast samples are displayed in Fig. 2 and S4,† respectively. For the low SAR system, the two contrast samples show obviously low crystallinity as compared with SSZ-1334.1, although their crystallization took a much longer time. Meanwhile, the SEM images also evidence the existence of many amorphous particles in both contrast A_{34.1} and B_{34.1}. For the high SAR system, the difference between contrast samples and SSZ-1396.1 becomes more evident, confirming the increased difficulty for the synthesis of the high-

Table 1 Synthesis conditions, product properties and yields of SSZ-13

Sample	Gel composition				Crystallization conditions		Product		
	m^a	n^a	x^b	y^b	T (°C)	Time (h)	Phase	SAR^c	Yield ^d (%)
SSZ-13 _{23.2}	23.8	0.009	24.0	0.035	175	12	СНА	23.2	92.8
SSZ-13 _{34.1}	38.0	0.014	36.1	0.040	175	6	CHA	34.1	91.9
SSZ-13 _{47.1}	57.0	0.014	50.7	0.040	175	6	CHA	47.1	92.9
SSZ-13 _{69.1}	95.0	0.020	74.9	0.045	175	10	CHA	69.1	92.3
SSZ-13 _{96.1}	190.0	0.025	116.6	0.050	175	10	CHA	96.1	82.8
SSZ-13 _{am}	∞	0.025	264.0	0.050	175	24	CHA + amor.	_	_
SSZ-13 _{33.2}	38.0	0.014	36.1	0.040	195	3	CHA	33.2	92.0
SSZ-13 _{31.5}	38.0	0.014	36.1	0.040	205	1.5	CHA	31.5	87.3

 $[^]a$ Initial gel before the addition of embryonic-CHA-zeolite solution: 1 SiO $_2$: 1/m Al $_2$ O $_3$: 0.053 Na $_2$ O: n TMAdaOH: 27 H $_2$ O. b Final gel for the crystallization of SSZ-13: 1 SiO₂: 1/x Al₂O₃: 0.048 Na₂O: y TMAdaOH: 20.6 H₂O, which contains the sources from the embryonic-CHA-zeolite solution (10% addition, based on SiO₂). c Product SiO₂/Al₂O₃ determined by XRF. d Yield was determined by the mass of silica and alumina.

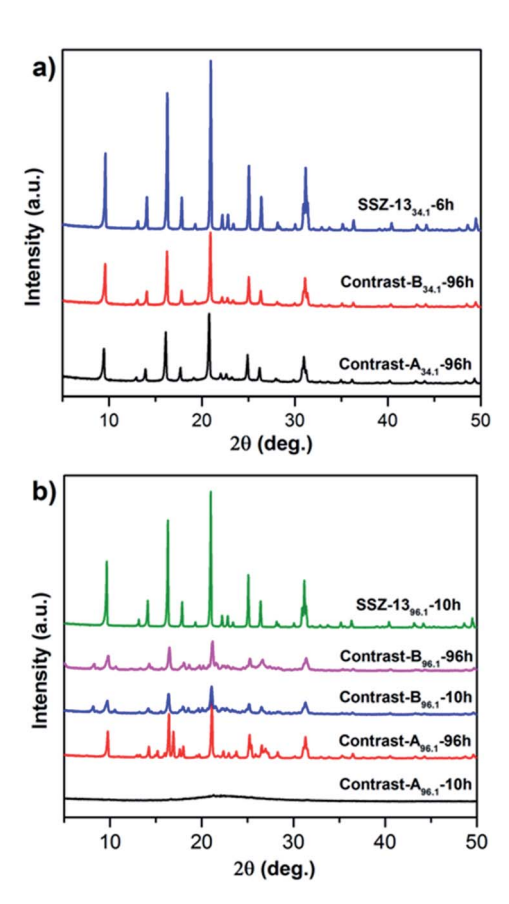


Fig. 2 XRD patterns of (a) SSZ-13 $_{34.1}$, (b) SSZ-13 $_{96.1}$ and their contrast samples. Contrast A: without the addition of embryonic-CHA-zeolite solution; contrast B: using H-SSZ-13 seeds in place of embryonic-CHA-zeolite solution. The final gel compositions in (a) and (b) were controlled to be the same as those of SSZ-13 $_{34.1}$ and SSZ-13 $_{96.1}$, respectively.

silica sample. The crystallization of contrast $A_{96.1}$ was quite slow. When its crystallization time was prolonged to 96 h, some amorphous material still existed accompanied by the formation of some impurity. For contrast $B_{96.1}$, STT impurity appeared together with SSZ-13 after 10 h, which showed little change until 96 h. These results clearly evidenced that the embryonic crystals play a crucial role in the fast and efficient synthesis of SSZ-13.

Characterization of SSZ-13

Sample SSZ- $13_{34.1}$ was chosen for various characterizations (Fig. 1 and 3). The XRD pattern of SSZ- $13_{34.1}$ (Fig. 1a) exhibits

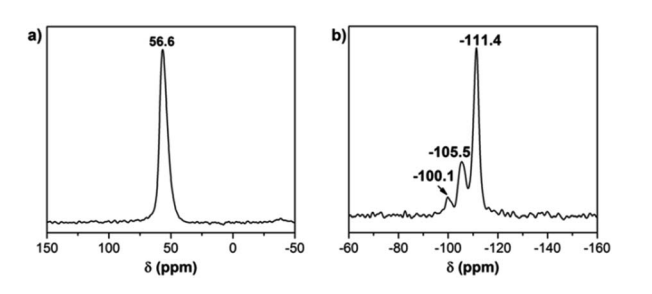


Fig. 3 (a) $^{27}\mathrm{Al}$ and (b) $^{29}\mathrm{Si}$ MAS NMR spectra of the as-made sample SSZ-13 $_{34.1}.$

well resolved characteristic diffraction peaks of the CHA-type structure without impurities. N2 sorption isotherm was used to test the pore structure of the calcined SSZ-1334.1. A typical Langmuir-type curve was observed at $10^{-6} < P/P_0 < 0.01$ (Fig. 1c), corresponding to the micropores in this material. The BET surface area and pore volume are 0.30 cm³ g⁻¹ and 596 cm² g⁻¹, respectively, which are comparable to those of high silica SSZ-13 reported before.34 The 27Al and 29Si MAS NMR spectra of SSZ- $13_{34.1}$ are illustrated in Fig. 3a and b, respectively. The 27 Al NMR spectrum contains only one sharp peak at 56.6 ppm, showing the regular state of tetrahedral-coordinated Al species in the framework.15 Two strong resonances centered at -111.4 and -105.5 ppm dominate in the ²⁹Si spectrum, which could be assigned to Si(4Si0Al) and Si(3Si1Al) species, respectively. The signal at -100 ppm could be assigned to Si(3Si)OH (O^3), arising from the defects mentioned in the previous studies. 45 Thus the SAR deduced from the ²⁹Si MAS NMR is in good agreement with the composition determined by XRF. Moreover, there are four resonance signals in the solid ¹³C MAS NMR spectrum (Fig. 1d), which arises from the C species of TMAda⁺, evidencing that the TMAda⁺ remained intact in the CHA cages of SSZ-13.³³

Crystallization processes of SSZ-13 with different SARs

The crystallization processes of SSZ-13 with different gel SARs under the assistance of embryonic-CHA-zeolite solution were traced and the results are displayed in Fig. 4 and 5. It is clear that all the three systems present characteristics of fast crystallization, which is complete in 12 h. However, there also exist obvious differences among the systems. More specifically, the system of SSZ-13_{23.2} with a relatively low gel SAR has a longer induction period of 8 h; no obvious induction period can be observed for the crystallization of SSZ-13_{34.1}, and its solid product is fully crystallized after 4 h with a high yield of 90.8%. When the gel SAR further increases, the induction period is still inconspicuous, but its crystal growth rate becomes slow as compared to the other two systems.

Previous studies have demonstrated that the content of Al species in the gel determines the nucleation rate and the number of nuclei, and ultimately affects the product morphology and yield.^{15,46} The crystallization of SSZ-13 with

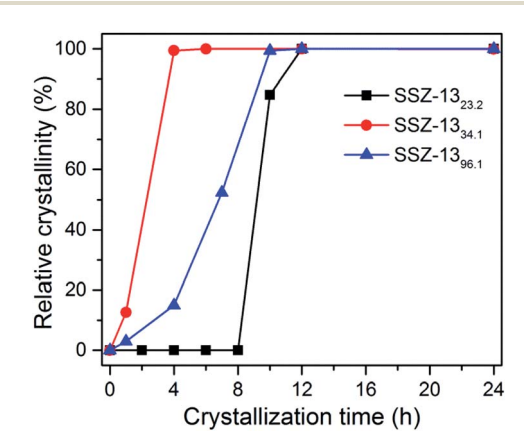


Fig. 4 Crystallization curves of SSZ-13s with different gel SARs.



Fig. 5 SEM images of SSZ-13s with different gel SARs.

a low SAR needs more crystal nuclei, which may follow a nonclassical mechanism47 and gives products with spherical morphology and a rough surface. This is consistent with the longer induction period and crystal morphology observed for SSZ-13_{23.2} (Fig. 5). For the sample with a relatively high SAR, the crystallites tend to grow in a classical layer-by-layer mode, resulting in crystals with cube-like morphology and larger size, as presented for SSZ-1334.1 and SSZ-1396.1 (Fig. 5). Moreover, the relatively slow crystal growth rate of SSZ-1396.1 also indicates the difficulty in the formation of the high-silica CHA framework.

Catalytic performance in NH₃-SCR and MTO reactions

Sample SSZ-1323.2 with a relatively low SAR was used as a precursor for the preparation of the Cu-SSZ-13 catalyst. The Cu content was measured to be 2.41 wt% (Cu: Al = 0.275, ion exchange level of 55%). Fig. 6 displays the dependence of the NH₃-SCR catalytic activity on reaction temperature over Cu-SSZ-13_{23.2}. The fresh catalyst displays NO_x conversion of \sim 100% in a wide temperature range of 200-450 °C at a large GHSV of 300 000 h⁻¹. When the reaction temperature increases to 550 °C, a respectable conversion of 93.7% could still be observed, evidencing the superior catalytic activity of Cu-SSZ-1323.2. Given that the high-temperature hydrothermal stability of Cu-SSZ-13 is vital for its practical application, the NH₃-SCR catalytic properties of hydrothermally aged Cu-SSZ-1323,2 are further investigated and shown in Fig. 6. The NO_x conversion

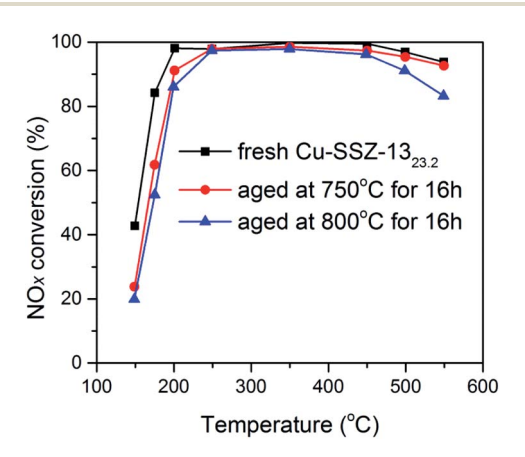


Fig. 6 NO_x conversion as a function of temperature on fresh and hydrothermally aged Cu-SSZ-13_{23.2}. Feed gas: NO (0.05%), NH₃ (0.05%), H₂O (6.4%), O₂ (6.4%) and N₂. GHSV = 300 000 h⁻¹.

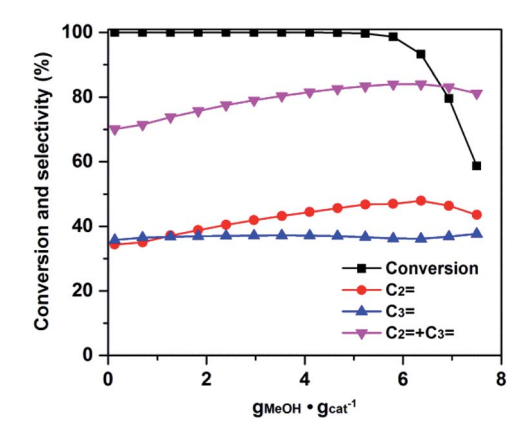


Fig. 7 Conversion and product selectivity as a function of methanol throughput on H-SSZ-13_{96.1}. Reaction conditions: 400 °C, atmospheric pressure, CH_3OH WHSV = 2 h^{-1}

remains higher than 90% in the range of 200-550 $^{\circ}\text{C}$ after treatment at 750 °C for 16 h. Even after a harsher treatment at 800 °C, more than 95% conversion could be achieved in the range of 250-450 °C, suggesting the excellent hydrothermal stability of the Cu-SSZ- $13_{23.2}$ catalyst.

Furthermore, high-silica SSZ-1396.1 was also tested as an MTO catalyst to investigate its catalytic performance. The reaction results are displayed in Fig. 7. Under the studied conditions, H-form SSZ-1396.1 shows a methanol throughput of $5.2 \text{ g}_{\text{MeOH}} \text{ g}_{\text{cat}}^{-1}$ in its lifetime (>99.5% methanol conversion). The initial selectivity of ethene plus propene is 70.1 wt%, which increases gradually to 83.5 wt% until the catalyst deactivation. This result is also comparable to or even better than the catalytic performance of high-silica SSZ-13 reported previously (synthesized with a large amount of TMAdaOH, TMAdaOH/SiO₂ = 0.2),15,19 which implies the good quality of the high-silica SSZ-13 synthesized by the embryonic zeolite-assisted method.

Besides the success in the synthesis of SSZ-13, another industrially important zeolite TS-1 (MFI topology) has also been efficiently synthesized by utilizing the embryonic zeoliteassisted strategy. The specific information will be reported in detail in the future.

Conclusions

In summary, we have developed a facile embryonic zeoliteassisted strategy for the highly efficient synthesis of zeolites. Based on this strategy, SSZ-13 has been successfully synthesized under ultra-low OSDA usage with a fast crystallization rate, wide SAR range and high solid yields. It is revealed that the X-ray amorphous embryonic CHA zeolite has a nanometer size, large pore volume and abundant D6R units, which contributes to the fast synthesis of SSZ-13. In addition, SSZ-13 synthesized from different gel SARs is found to have distinct crystallization rates, leading to different morphologies and crystal sizes. The resultant SSZ-13_{23.2}, after Cu²⁺ exchange, displays excellent NH₃-SCR activity and high-temperature hydrothermal stability, which promises its practical application for the NH₃-SCR process. High-silica SSZ-13_{96.1} is explored as a catalyst for the MTO reaction, which also presents good catalytic performance. This facile strategy offers an alternative to other costly and complicated routes for the synthesis of SSZ-13, and holds potential for the efficient synthesis of more industrially important zeolites.

Author contributions

The manuscript was completed through the contributions of all authors. All authors have given approval to the final version of the manuscript. Linying Wang carried out the experiments and wrote the draft. Dali Zhu and Juan Wang took part in some of the synthesis experiments. Wenhao Cui participated in parts of the characterizations. Jingfeng Han carried out the UV-Raman test. Bing Li tested the MTO performances. Peng Tian and Zhongmin Liu guided the research project. Peng Tian and Dong Fan modified the manuscript.

Conflicts of interest

There are no conflicts to declare.

Acknowledgements

The authors acknowledge the National Natural Science Foundation of China (No. 21991090 and 21991091) and the Key Research Program of Frontier Sciences, Chinese Academy of Sciences (Grant No. QYZDB-SSW-JSC040) and DICP Funding (DICP ZZBS201807).

Notes and references

- 1 A. Corma, Chem. Rev., 1997, 97, 2373-2419.
- 2 V. Van Speybroeck, K. Hemelsoet, L. Joos, M. Waroquier, R. G. Bell and C. R. A. Catlow, *Chem. Soc. Rev.*, 2015, 44, 7044–7111.
- 3 M. Dusselier and M. E. Davis, *Chem. Rev.*, 2018, **118**, 5265–5329.
- 4 M. E. Davis and R. F. Lobo, Chem. Mater., 1992, 4, 756-768.
- 5 V. Nikolakis, Curr. Opin. Colloid Interface Sci., 2005, 10, 203-210.

- 6 X. Meng and F. S. Xiao, Chem. Rev., 2014, 114, 1521-1543.
- 7 D. K. Pappas, E. Borfecchia, M. Dyballa, I. A. Pankin, K. A. Lomachenko, A. Martini, M. Signorile, S. Teketel, B. Arstad, G. Berlier, C. Lamberti, S. Bordiga, U. Olsbye, K. P. Lillerud, S. Svelle and P. Beato, *J. Am. Chem. Soc.*, 2017, 139, 14961–14975.
- 8 R. Oord, J. E. Schmidt and B. M. Weckhuysen, *Catal. Sci. Technol.*, 2018, **8**, 1028–1038.
- 9 A. Koishybay and D. F. Shantz, J. Am. Chem. Soc., 2020, 142, 11962–11966.
- A. M. Beale, F. Gao, I. Lezcano-Gonzalez, C. H. Peden and J. Szanyi, *Chem. Soc. Rev.*, 2015, 44, 7371–7405.
- 11 F. Gao, N. M. Washton, Y. Wang, M. Kollár, J. Szanyi and C. H. F. Peden, J. Catal., 2015, 331, 25–38.
- 12 J. Zhang, Y. Shan, L. Zhang, J. Du, H. He, S. Han, C. Lei, S. Wang, W. Fan, Z. Feng, X. Liu, X. Meng and F.-S. Xiao, *Appl. Catal.*, B, 2020, 277, 119193–119200.
- 13 S. Zhang, L. Pang, Z. Chen, S. Ming, Y. Dong, Q. Liu, P. Liu, W. Cai and T. Li, *Appl. Catal.*, A, 2020, 607, 117855–117876.
- 14 F. Bleken, M. Bjørgen, L. Palumbo, S. Bordiga, S. Svelle, K.-P. Lillerud and U. Olsbye, *Top. Catal.*, 2009, 52, 218–228.
- 15 Q. Zhu, J. N. Kondo, R. Ohnuma, Y. Kubota, M. Yamaguchi and T. Tatsumi, *Microporous Mesoporous Mater.*, 2008, **112**, 153–161.
- 16 U. Deka, A. Juhin, E. A. Eilertsen, H. Emerich, M. A. Green, S. T. Korhonen, B. M. Weckhuysen and A. M. Beale, *J. Phys. Chem. C*, 2012, 116, 4809–4818.
- 17 Z. Liu, T. Wakihara, K. Oshima, D. Nishioka, Y. Hotta, S. P. Elangovan, Y. Yanaba, T. Yoshikawa, W. Chaikittisilp, T. Matsuo, T. Takewaki and T. Okubo, *Angew. Chem., Int. Ed. Engl.*, 2015, 54, 5683–5687.
- 18 Z. Liu, N. Nomura, D. Nishioka, Y. Hotta, T. Matsuo, K. Oshima, Y. Yanaba, T. Yoshikawa, K. Ohara, S. Kohara, T. Takewaki, T. Okubo and T. Wakihara, *Chem. Commun.*, 2015, 51, 12567–12570.
- 19 I. Yarulina, A. Dikhtiarenko, F. Kapteijn and J. Gascon, *Catal. Sci. Technol.*, 2017, 7, 300–309.
- 20 J. Han, X. Jin, C. Song, Y. Bi, Q. Liu, C. Liu, N. Ji, X. Lu, D. Ma and Z. Li, *Green Chem.*, 2020, 22, 219–229.
- 21 Y. Lv, C. Ye, J. Zhang and C. Guo, *Microporous Mesoporous Mater.*, 2020, **293**, 1–8.
- 22 Y. Guo, T. Sun, X. Liu, Q. Ke, X. Wei, Y. Gu and S. Wang, *Chem. Eng. J.*, 2019, **358**, 331–339.
- 23 M. J. Diaz-Cabanas, P. A. Barrett and M. A. Camblor, *Chem. Commun.*, 1998, 17, 1881–1882.
- 24 Z. Pourmahdi and H. Maghsoudi, *Adsorption*, 2017, 23, 799–807.
- 25 S. I. Zones, J. Chem. Soc., Faraday Trans., 1990, 86, 3467–3472.
- 26 L. Tang, K.-G. Haw, Y. Zhang, Q. Fang, S. Qiu and V. Valtchev, *Microporous Mesoporous Mater.*, 2019, 280, 306–314.
- 27 S. I. Zones, J. Chem. Soc., Faraday Trans., 1991, 87, 3709–3716.
- 28 M. Itakura, I. Goto, A. Takahashi, T. Fujitani, Y. Ide, M. Sadakane and T. Sano, *Microporous Mesoporous Mater.*, 2011, 144, 91–96.

- 29 L. Ren, L. Zhu, C. Yang, Y. Chen, Q. Sun, H. Zhang, C. Li, F. Nawaz, X. Meng and F. S. Xiao, Chem. Commun., 2011, 47, 9789-9791.
- 30 B. Chen, R. Xu, R. Zhang and N. Liu, Environ. Sci. Technol., 2014, 48, 13909-13916.
- 31 N. Martin, M. Moliner and A. Corma, Chem. Commun., 2015, 51, 9965-9968.
- 32 X. Wang, Q. Wu, C. Chen, S. Pan, W. Zhang, X. Meng, S. Maurer, M. Feyen, U. Muller and F. S. Xiao, Chem. Commun., 2015, 51, 16920-16923.
- 33 Y. Yamasaki, N. Tsunoji, Y. Takamitsu, M. Sadakane and T. Sano, Microporous Mesoporous Mater., 2016, 223, 129-139.
- 34 X. Xiong, D. Yuan, Q. Wu, F. Chen, X. Meng, R. Lv, D. Dai, S. Maurer, R. McGuire, M. Feyen, U. Müller, W. Zhang, T. Yokoi, X. Bao, H. Gies, B. Marler, D. E. De Vos, U. Kolb, A. Moini and F.-S. Xiao, J. Mater. Chem. A, 2017, 5, 9076-9080.
- 35 K.-G. Haw, J.-P. Gilson, N. Nesterenko, M. Akouche, H. El Siblani, J.-M. Goupil, B. Rigaud, D. Minoux, J.-P. Dath and V. Valtchev, ACS Catal., 2018, 8, 8199-8212.
- 36 R. Bai, M. T. Navarro, Y. Song, T. Zhang, Y. Zou, Z. Feng, P. Zhang, A. Corma and J. Yu, Chem. Sci., 2020, 11, 12341-12349.

- 37 S. Inagaki, K. Thomas, V. Ruaux, G. Clet, T. Wakihara, S. Shinoda, S. Okamura, Y. Kubota and V. Valtchev, ACS Catal., 2014, 4, 2333-2341.
- 38 Y. Cao, D. Fan, L. Sun, M. Yang, L. Cao, T. Sun, S. Xu, P. Tian and Z. Liu, Chem. Eng. J., 2019, 374, 832-839.
- 39 F. Fan, Z. Feng, K. Sun, M. Guo, Q. Guo, Y. Song, W. Li and C. Li, Angew. Chem., Int. Ed. Engl., 2009, 48, 8743-8747.
- 40 O. Attila, H. E. King, F. Meirer and B. M. Weckhuysen, Chem.-Eur. J., 2019, 25, 7158-7167.
- 41 J. Zhang, Y. Chu, X. Liu, H. Xu, X. Meng, Z. Feng and F.-S. Xiao, Chin. J. Catal., 2019, 40, 1854-1859.
- 42 C. Sun, D. J. Srivastava, P. J. Grandinetti and P. K. Dutta, Microporous Mesoporous Mater., 2016, 230, 208-216.
- 43 D. Zhu, L. Wang, D. Fan, N. Yan, S. Huang, S. Xu, P. Guo, M. Yang, J. Zhang, P. Tian and Z. Liu, Adv. Mater., 2020, 32, DOI: 10.1002/adma.202000272.
- 44 Z. Sheng, H. Li, K. Du, L. Gao, J. Ju, Y. Zhang and Y. Tang, Angew. Chem., Int. Ed., 2021, 60(24), 13444-13451.
- 45 E. A. Eilertsen, B. Arstad, S. Svelle and K. P. Lillerud, Microporous Mesoporous Mater., 2012, 153, 94-99.
- 46 Z. Xu, H. Ma, H. Zhang, W. Qian and W. Ying, International Scholarly and Scientific Research & Innovation, 2018, 12(10), 531-535.
- 47 M. Kumar, H. Luo, Y. Roman-Leshkov and J. D. Rimer, J. Am. Chem. Soc., 2015, 137, 13007-13017.